Structural hierarchy as a key to complex phase selection in Al-Sm

Z. Ye,[1,*] F. Zhang,[1,†] Y. Sun,[1,2] M. C. Nguyen,[1] S. H. Zhou,[1] L. Zhou,[1] F. Meng,[1] R. T. Ott,[1] E. Park,[1] M. F. Besser,[1] M. J. Kramer,[1] Z. J. Ding,[2] M. I. Mendelev,[1] C. Z. Wang,[1] R. E. Napolitano,[1,3] and K. M. Ho[1,4,2,‡]

[1]*Ames Laboratory, US Department of Energy, Ames, Iowa 50011, USA*

[2]*Hefei National Laboratory for Physical Sciences at the Microscale and Department of Physics, University of Science and Technology of China, Hefei, Anhui 230026, China*

[3]*Department of Materials Science and Engineering, Iowa State University, Ames, Iowa 50011, USA*

[4]*Department of Physics, Iowa State University, Ames, Iowa 50011, USA*

(Received 4 June 2017; published 12 October 2017)

Investigating the unknown structure of the complex cubic phase, previously observed to crystallize from melt-spun amorphous Al–10 at.% Sm alloy, we determine the structure in full site-occupancy detail, highlighting several critical structural features that govern the far-from-equilibrium phase selection pathway. Using an efficient genetic algorithm combining molecular dynamics, density functional theory, and x-ray diffraction, the structure is clearly identified as body-centered cubic $Im\bar{3}m$ (No. 229) with ∼140 atoms per cubic unit cell and a lattice parameter of 1.4 nm. The complex structure is further refined to elucidate the detailed site occupancy, revealing full Sm occupancy on 6b sites and split Sm/Al occupancy on 16f sites. Based on the refined site occupancy associated with the experimentally observed phase, we term this phase ε-$Al_{60}Sm_{11}$(bcc), corresponding to the limiting situation when all 16f sites are occupied by Sm. However, it should be recognized that the range of solubility enabled by split occupancy at Sm sites is an important feature in phase selection under experimental conditions, permitting an avenue for transition with little or no chemical partitioning. Our analysis shows that the ε-$Al_{60}Sm_{11}$(bcc) exhibits a "3-6-6-1" first-shell packing around Sm centers on 16f sites, the same dominant motif exhibited by the undercooled liquid. The coincident motif supports the notion that liquid/glass ordering at high undercooling may give rise to topological invariants between the noncrystalline and crystalline states that provide kinetic pathways to metastable phases that are not accessible during near-equilibrium processing.

DOI: 10.1103/PhysRevMaterials.1.055601

I. INTRODUCTION

Devitrification of amorphous metallic alloys typically involves passing through low-temperature regimes where multiple competing transitions are thermodynamically possible yet kinetic processes are limited. Multistep transition sequences are common, during which complex transient metastable structures may precipitate initially, in favor of more stable compounds [1–5]. The crystallization of some Zr- and Hf-based alloy glasses, for instance, includes the formation of a large-unit-cell (LUC) cubic phase (∼100 atoms) [1–4]. The competitiveness of high-symmetry LUC phases suggests a structural hierarchy and complex dynamics connecting short-range features with order on a much larger scale. During devitrification, the manifestation of hierarchical relationships may give rise to sequences of transient metastable structures, where the reaction pathway highlights the critical connections. In some cases, glassy alloys may relax to quasicrystals and their approximant complex LUC phases [1,6,7]. In other cases, devitrification sequences are dominated by the existence of low-energy phase boundary relationships that favor specific kinetic pathways [8,9]. Ordering in the undercooled parent liquid or glass may also be a major contributor, and considerable evidence has been reported to suggest that icosahedral or other forms of short to medium range order may strongly influence phase selection [9]. While the hierarchical connections between noncrystalline order and LUC phase selection have not been clearly established, we have reported specifically on the role of short-range packing motifs which may contribute to glassy behavior and may serve as precursors for particular crystalline phases in Cu-Zr and Al-Sm alloys [10,11].

Crystallization in such cases involves competition between multiple highly driven structural transitions, and kinetically favored reaction pathways may include states with a substantial number of crystal-chemical defects. Since quantification of the critical thermodynamic and kinetic factors surrounding these reactions requires explicit descriptions of the involved states, determination of complex LUC phases is central to understanding the pathway. Once the structures are known, various computational methods can be brought to bear to describe and probe the observed reactions and associated kinetics. Experimental determination of the detailed structure of these metastable LUC phases, however, is complicated by the nanoscale nature of precipitates that form under very high driving forces. In addition, highly driven transformations often involve accommodation of various defect structures and chemistries (e.g., vacancies, solutes, antisite occupancy defects, and stacking faults) where the associated energetic penalty is "traded" for a net enhancement of reaction kinetics. Reported attempts to identify complicated structures in glassy systems have been based almost exclusively on searching existing databases containing known prototype structures [3,12,13], and success has been limited.

*zye@iastate.edu
†fzhang@ameslab.gov
‡kmh@ameslab.gov

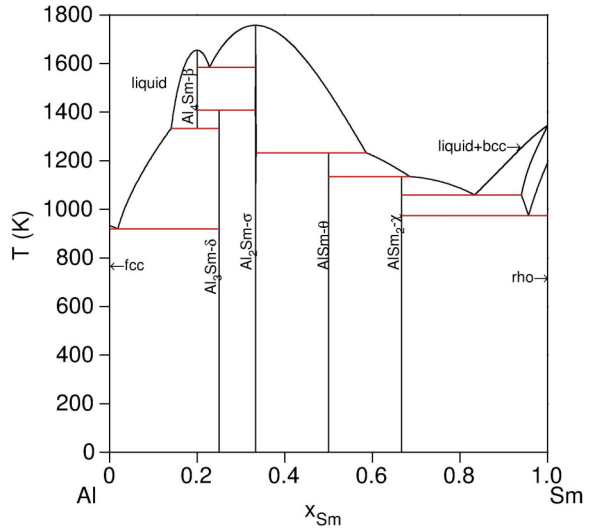

FIG. 1. The Al-Sm phase diagram [23].

In this paper, we employ a more general method using a combination of efficient genetic algorithm (GA) search guided by lattice parameters from high-energy x-ray diffraction data and subsequent molecular dynamics (MD) seeded growth simulation. We focus on the unresolved complex cubic LUC phase previously observed (termed MS1) during devitrification of glassy Al-Sm alloys [14–16]. We show that one of the principal short-range structures in the complex cubic phase is identical to the dominant cluster motif in the undercooled liquid. The coincident packing suggests a topological invariant in the short/medium range order that may provide a low-barrier kinetic pathway to the LUC phase. This hierarchical connection is further supported by our MD simulations of the liquid/crystal interface, revealing rapid growth in the undercooled state.

The Al-RE-TM alloys (RE and TM denote "rare earth" and "transition metal," respectively) comprise a class with promising combinations of high strength and low density [17]. Many of these alloys are glass formers, and the amorphous phase may be an important constituent in the final structure or may play a key role as in intermediate phase in the overall transition path. In some cases, far-from-equilibrium pathways provide an opportunity to realize phases and structures that are otherwise inaccessible [18]. As a marginal glass former exhibiting a broad glass-forming composition range [14,15,17,19,20], the Al-RE binary systems serve as prototypes for the investigation of these complex multistage crystallization sequences involving multiple unknown metastable phases and strong composition dependence [16,17,21,22].

TABLE I. Metastable phases in the Al-Sm system.

Phase Designator	Formula Unit (FU)	FUs per Unit cell	Space group	Prototype
η	$Al_{41}Sm_5$	2	$I4/m$	
ε	$Al_{60}Sm_{11}$	2	$Im\bar{3}m$	bcc
π	Al_5Sm	1	$P6/mmm$	Cu_5Ca
θ	Al_5Sm	4	$P6_3/mmc$	
β	Al_4Sm	1	$I4/mmm$	Al_4Ba
γ	Al_4Sm	3	$Imma$	Al_4U
α	$Al_{11}Sm_3$	1	$Immm$	$Al_{11}La_3$

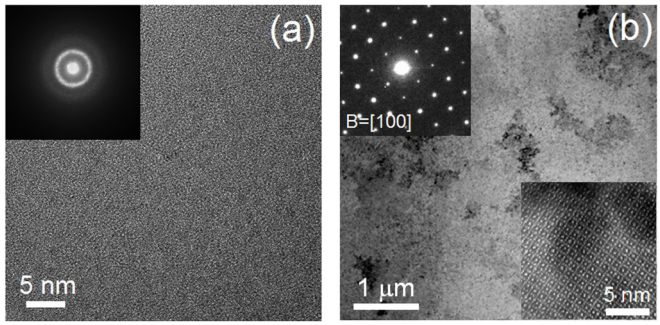

FIG. 2. Bright-field transmission electron microscopy (TEM) images of the (a) as-quenched Al–10 at.% Sm melt-spun ribbons, and the (b) ε-$Al_{60}Sm_{11}$ in Al–10 at.% Sm annealed at 470 K for 9 min. Inset: Corresponding selected area diffraction (SAD) pattern and high-resolution high-angle annular dark field (HAADF) image.

Al-Sm is an interesting system for which a glassy structure is readily attainable using conventional melt-spinning processes over compositions ranging generally from 7 to 13 at.% Sm [14,17,22,24]. Moreover, *in situ* high-energy x-ray diffraction experiments have shown [14,16,22] that many phases participate in complex devitrification sequences within this range, including the stable phases shown in Fig. 1 and the metastable phases listed in Table I. In this paper, we specifically address the complex cubic phase, first reported in 1994 [14], that appears in the initial crystallization step in Al–10 at.% Sm melt-spun ribbons before decomposing into multiple phases.[1] This phase was previously termed MS1 [14–16] and is termed ε-$Al_{60}Sm_{11}$ in this work, but the complex structure was never determined. A typical devitrification sequence exhibiting the ε-$Al_{60}Sm_{11}$ phase is shown Fig. 2, where the phase appears to nucleate and grow in a polycrystalline manner with no (observable) chemical partitioning.[2] Until the present, the atomic structure of the ε-$Al_{60}Sm_{11}$ phase remained unknown, preventing fundamental understanding of the initial selection of this LUC phase (∼140 atoms per unit cell) in favor of other simpler and more stable structures.

II. METHODOLOGY

Typically neutron or x-ray powder diffraction, sometimes in concert with transmission electron diffraction, is used to identify unknown crystalline structures in observed phases. However, a complex LUC phase with mixed or partial occupancy on one or more Wyckoff sites presents a major difficulty for structure identification from diffraction alone. Accordingly, we

[1]An "M2" phase also appears in the initial crystallization step in Al–10 at.% Sm ribbons as reported in Ref. [16], where detectable amounts of M2 phase and fcc-Al coexist with the amorphous phase before the devitrification.

[2]We qualify the description here because we cannot yet categorically rule out nanoscale chemical segregation during growth of this phase.

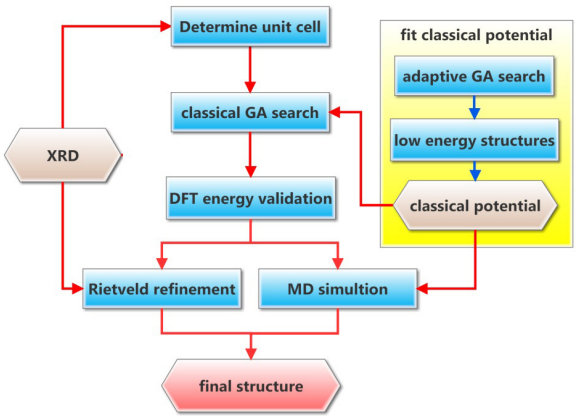

FIG. 3. A schematic flow diagram of our integrated approach.

employ here an integrated approach, combining synchrotron x-ray diffraction with Rietveld refinement, a GA search validated by density functional theory (DFT) calculations, and molecular dynamics simulations, to determine the detailed structure.

We schematically depict our integrated approach in Fig. 3. We first use the experimental diffraction patterns to deduce the lattice parameters and the space group symmetry. Then, we perform a global search for low-energy structures using a GA, with the constraints of the predetermined space group symmetry, which effectively reduces the size of the system and at the same time restricts the GA search to a subset of metastable structures that satisfy the experimental data. Even with the help of the symmetrization, it remains impractical to use straightforward first-principles calculations throughout the search for large unit cells. Thus, we use an efficient classical potential for energy calculations during the GA search. To ensure its accuracy, the classical potential has been preadapted in GA searches on smaller cells, using procedures described in Ref. [1]. A more accurate first-principles density function theory (DFT) energy is calculated for the first 16 low-energy structures in the converged GA pool. All DFT calculations [25] are performed using the Vienna *ab initio* simulation package (VASP) [26] with the projector-augmented wave (PAW) pseudopotential method [27,28] within the generalized-gradient approximation (GGA) [29]. Since the full space group symmetry is enforced throughout the search, the final structures have full occupancies for all the Wyckoff positions. In order to account for possible random vacancies or antisites associated with partial occupancies, the best candidates from the DFT calculations are fed to a Rietveld analysis, in which the lattice parameters, atomic coordinates, and site occupancies are fine-tuned to obtain an optimal match between the experimental and calculated diffraction patterns. Since physical guidelines are limited in the Rietveld analysis, to ensure that it does not result in unphysical results, we finally perform a large-scale molecular dynamics simulation on the transformation from the amorphous to the crystalline phases. The newly grown crystalline phase can help confirm whether the antisites predicted in the Rietveld analysis are realistic.

III. RESULTS AND DISCUSSION

The ε-$Al_{60}Sm_{11}$ phase was previously reported to be cubic with a lattice parameter of ∼9.8 Å [16]. Our present high-energy x-ray diffraction experiments, however, do not support this, yielding multiple diffraction peaks not attributable to the primitive cubic cell [30]. Rather, detailed analysis clearly reveals a body-centered cubic structure with a lattice parameter of ∼13.9 Å and an estimated ∼140 atoms/unit cell (based on the simple assumption of density similar to that of the glass (51 atoms/nm^3). Determination of the atomic-site positions and site-occupancies from x-ray diffraction fine-structure analysis is not possible without having considerable *a priori* knowledge of the structure. Using the experimental unit-cell information, we perform a GA search for low-energy crystal structures with varying Al-Sm compositions.

GA techniques are well established [31,32] and are based on the principles of evolution in biological systems, utilizing numerical operations analogous to crossover, mutation, and natural selection. By defining *fitness* (i.e., survival likelihood or viability) as a function of formation energy, GA methods have reliably identified low-energy structures and have successfully predicted observed phases [33–37]. In our approach, the global search is efficiently conducted by performing structure relaxations using the LAMMPS code [38] with an embedded-atom method (EAM) potential in the Finnis-Sinclair (FS) formulation [39]. As previously shown [33,40], by tuning to first-principles calculation results, this FS potential generally provides reasonable estimates of relative thermodynamic stability, allowing comparison between the known stable and metastable phases.

Low-energy structures from the GA pool were further relaxed using more accurate first-principles density functional theory (DFT) calculations. The structure with the lowest formation energy has space group $Im\bar{3}m$ (No. 229). The structure includes six unique Wyckoff positions (see Table II) and an $Al_{120}Sm_{22}$ stoichiometry. We hereafter refer to this phase as ε-$Al_{60}Sm_{11}$(bcc). Under experimental conditions, variable occupancy of Sm sites allows a wide range of solubility, permitting an avenue for transition with little or no chemical partitioning.

Since the $Al_{60}Sm_{11}$ crystal structure has Sm concentration (15.5%) which is considerably different from the experimentally observed phase (10%), a Rietveld refinement [41,42] was carried out using the GSAS package and the EXPGUI interface [43] to determine the site occupancies. In this method, lattice parameter, atomic coordinates, site occupancies, thermal parameters, and peak shape profiles are refined simultaneously. The refined structure is shown in Fig. 4, and the corresponding computed XRD pattern is compared with experiment. As shown in the inset of Fig. 4(a), the atomic structure is in good agreement with the high-resolution TEM image. The refined atomic coordinates and fitted occupancies are listed in Table II. Excellent match with experiment is achieved when the Sm/Al site (16f) is evenly shared by Sm and Al (assuming the Sm/Al site to be fully occupied by Sm alone has a much poorer fit). To distinguish the fully occupied (6b) and shared (16f) Sm sites, they are marked in Figs. 4(a) and 4(b) with blue and yellow, respectively. We highlight here the first shell packing environments around the full and partially occupied Sm sites,

TABLE II. Lattice parameters and atomic coordinates of the ε-$Al_{60}Sm_{11}$(bcc) phase based on the DFT and Rietveld analysis. Fitted values to the experimental observed phase are shown in parentheses. The fitting of the experimental data gives wRp = 0.062 and Rp = 0.049.

Lattice parameters (in units of Å) $\boldsymbol{a}$ = 13.904 (14.06)					
	Atomic coordinates and site occupancies				
	x	*Y*	*Z*	Wyckoff	Occupancies
Al(1)	0	0.143 (0.142)	0.316 (0.302)	48j	1
Al(2)	0.849 (0.845)	0	0	12e	1
Al(3)	0.25	0	0.5	12d	1
Al(4)	0.171 (0.164)	0.171 (0.164)	0.406 (0.405)	48k	1
Sm(1)	0	0.5	0.5	6b	1
Sm-Al	0.335 (0.328)	0.335 (0.328)	0.335 (0.328)	16f	1/0 (0.5/0.5)

which are termed here as 1-6-6-6-1 and 3-6-6-1 motifs, respectively, as illustrated with blue and yellow polyhedra in Figs. 4(b)–4(d). It is important to note further that we have previously shown that the 3-6-6-1 motif is the dominant cluster motif in the undercooled Al–10 at.% Sm liquid.

While the ε-$Al_{60}Sm_{11}$(bcc) structure described above is in excellent agreement with the experimental XRD data, it does not really prove that the Al/Sm antisite defects indicated by Rietveld analysis are realistic. It is well known that overfitting (i.e., fitting to noise or experimental error by utilizing too many fitting parameters) can occur in Rietveld analysis, which can lead to unphysical solutions of the structures. To study the nature of the native antisite defects and their effects on the growth of ε-$Al_{60}Sm_{11}$, we perform a large-scale (~3800 atoms) MD simulation using the same classical potential that successfully identified the ε-$Al_{60}Sm_{11}$(bcc) structure. We use a slab geometry with a square cross section, one long dimension, and periodic boundaries. The initial condition includes a template of the refined ε-$Al_{60}Sm_{11}$ structure contained within the liquid alloy of composition Al–10 at.% Sm. The geometry of the template is a slab with interfaces normal to the long axis of the simulation domain. The crystalline template is altered to have a mixed-occupancy 16f site, as predicted by Rietveld analysis [Fig. 5(a)]. Since the MD simulation of the crystal growth can be very computationally expensive, it is performed at an elevated temperature of 800 K to further expedite the formation of the ε phase (the devitrification of this alloy is experimentally observed at ~470 K). At 800 K, the crystal grows to fill the simulation domain within 280 ns, as shown in Fig. 5(b). Although the ε-$Al_{60}Sm_{11}$ is metastable with a positive formation energy with respect to Al(fcc) and Al_3Sm, it did not decompose into stable phases within the time frame of the MD simulations. Comparison between experimental XRD patterns and those computed[3] from the simulated crystals show excellent agreement with no additional fitting of atom positions or site occupancies [Fig. 5(c)]. This agreement indicates that the simulated crystal structure is realistic.

Looking more closely at the structure of the ε phase, Fig. 6(a) shows a comparison between the average atom positions obtained from the Rietveld analysis and MD simulation. Here we see that both methods indicate a cubic sublattice of 6b sites that is fully occupied by Sm (blue) atoms, forming a backbone for the structure. The 16f sites are mixed Al/Sm occupancy, shown as two-color spheres in Fig. 6(a). The MD structures in Figs. 6(b)–6(f) show specific examples of atomic positions, rather than the average positions shown in Fig. 6(a). These images explicitly show antisite defects as well as significant deviation from the average positions. Considering this tolerance for such imperfections to be a potential key for the selection of this complex phase, we compute the formation energy of the Al/Sm antisite defect on the 16f (yellow)

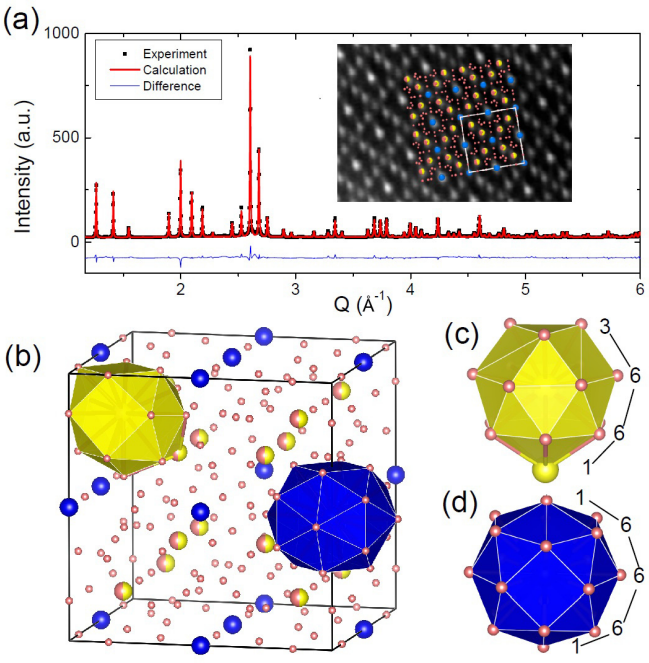

FIG. 4. The determined structure of the ε-$Al_{60}Sm_{11}$(bcc) phase. (a) Fitted XRD pattern with inset comparing the refined structure with the high-resolution TEM image taken on the [100] zone axis (Al, pink; Sm, blue/yellow). (b) Refined ε-$Al_{60}Sm_{11}$(bcc) unit cell showing two Sm-centered motifs: (c) the 3-6-6-1 motif, and (d) the 1-6-6-6-1 motif. The 3-6-6-1 motif is the dominant motif in the undercooled liquid.

[3]To get the XRD pattern of the simulated crystal growth from MD simulation [45] in Fig. 5(c), we first use Diamond software to calculate the XRD peak intensities from a snapshot of the simulated crystal growth and add a Gaussian function to the pattern. The lattice parameter and the Gaussian rms width are optimized with respect to experimental data.

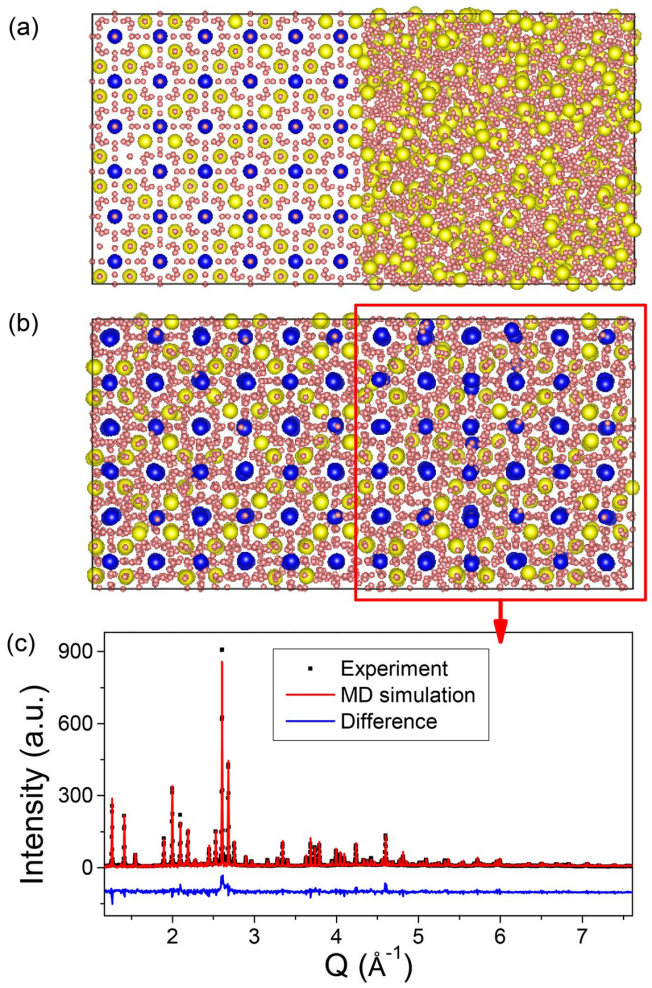

FIG. 5. MD simulation results. (a) Refined structure ε-$Al_{60}Sm_{11}$ in Fig. 4 serves as a seed (left part) to grow the crystalline structure from undercooled Al–10 at.% Sm liquids (right part). (b) The ε-$Al_{60}Sm_{11}$(bcc) structure is fully grown within 300 ns. The Sm atoms (blue) outline the cubic frame, with randomly distributed Sm-Al antisites (yellow). (c) The XRD pattern of the grown structure compared with experiment.

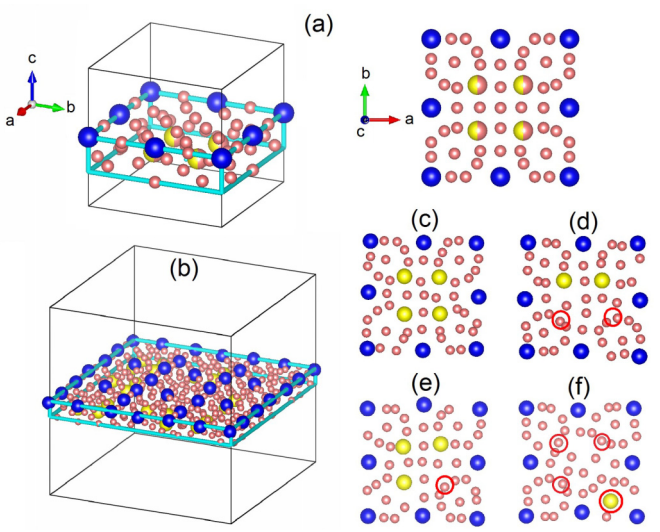

FIG. 6. A comparison of defects suggested by Rietveld analysis and by MD simulations. (a) A slice with a thickness of $a/4$ of the structure suggested by Rietveld analysis. (b) A slice with the same thickness from the grown 3 × 3 × 3 supercell structure. (c)–(f) Different locations in the slice shown in Fig. 6(b) to provide a close look of the 16f defects as marked in the red circle.

and 6b (blue) sites to be 0.6 and 1.2 eV, respectively. The comparative low energy of the 16f antisite defect is consistent with our XRD/Rietveld and MD findings, both revealing these defects only on the 16f sites. Low-energy accommodation of these defects provides a mechanism for Sm solubility and deviation from the strict $Al_{60}Sm_{11}$ stoichiometry, promoting selection of this phase over a range of compositions. The upper bound of this compositional range would be given by full Sm occupancy on the 16f sites, which correlates to a composition of Al–15.5 at.% Sm ($Al_{60}Sm_{11}$).

We now discuss why the ε-$Al_{60}Sm_{11}$(bcc) phase is initially selected in favor of simpler more stable phases (e.g., fcc-Al and $Al_{11}Sm_3$). In our MD simulations, the crystal structures are fully grown within 110 ∼ 280 ns. This high growth speed of ∼1 cm/s at a reduced temperature $T/T_m = 0.84$ for a structure with such a large unit cell is remarkable. In contrast, the thermodynamically stable and structurally simpler fcc-Al phase hardly grows under similar simulation conditions. One obvious advantage of the (near) polymorphic transition is that it requires little or no chemical partitioning and associated diffusion. This is in sharp contrast to the more stable phases in this system (e.g., fcc-Al, π-Al_5Sm, β-Al_4Sm, and Al_3Sm), which all require substantial partitioning to grow from the Al–10 at.% Sm glass.

Beyond partitioning and long-range diffusion, requirements for short-range ordering at a moving interface have been shown to dramatically reduce interface mobility. For example, MD simulations have shown that even the very simple B2 phase (containing only 2 atoms in the unit cell) grows from the liquid several orders of magnitude slower than the rate of solidification in pure metals [44]. In the case of the ε-$Al_{60}Sm_{11}$(bcc) phase, the easy accommodation of Al/Sm antisite defects may alleviate the requirement for interfacial ordering at the moving crystal-glass interface, substantially enhancing growth kinetics, favoring selection of this phase. This is consistent with prior TEM analysis of partially devitrified Al–10 at.% Sm glass, which revealed low nucleation rate and high growth rate characteristics of the glass to ε-$Al_{60}Sm_{11}$(bcc) transition.

Finally, we have described the clear structural connection between the dominant nanoscale order in the undercooled liquid and prevalent polyhedra within this crystalline phase. Specifically, 57% of the Sm-centered clusters in the ε-$Al_{60}Sm_{11}$(bcc) phase exhibit the 3-6-6-1 motif [Figs. 4(b) and 4(c)]. Moreover, our recent cluster-alignment analysis [11] has revealed the same dominant motif in undercooled Al–10 at.% Sm liquids, for which the ε-$Al_{60}Sm_{11}$(bcc) phase has been observed as the initial crystalline phase to form during the devitrification of amorphous ribbons produced by melt spinning. Combined with the vanishing diffusional burden associated with chemical partitioning and/or correction of site-occupancy defects, this structural invariant provides a low-barrier pathway to the complex ε-$Al_{60}Sm_{11}$(bcc) phase.

IV. CONCLUSION

In summary, using a genetic algorithm in conjunction with high-resolution x-ray diffraction experiments, we explicitly identify the complex and previously unidentified structure of the metastable cubic phase, which initially crystallizes from the amorphous Al–10 at.% Sm alloy. The structure is found to be body-centered cubic with space group $Im\bar{3}m$ (No. 229) with 142 atoms per cubic unit cell ($Al_{120}Sm_{22}$) and with 6 unique Wyckoff positions. Elucidation of the detailed structure of the large-unit-cell phase, termed here as ε-$Al_{60}Sm_{11}$(bcc), reveals a prevalent Sm-centered polyhedron motif that is coincident with the dominant motif predicted in the undercooled liquid/glass structure. This suggests a topological invariant linking the ε-$Al_{60}Sm_{11}$(bcc) phase with the parent glass, providing a kinetic pathway that may be critical to phase selection. In addition, the ε-$Al_{60}Sm_{11}$(bcc) phase is found to contain a substantial number of antisite defects, and the associated range of solubility enables the transition to proceed with little or no observable partitioning and diffusion. MD simulation and Rietveld analysis are used to investigate the nature of these defects and the associated kinetic effects. Together, these factors contribute substantially to the energetic and kinetic selection of this phase during initial devitrification, in favor of the more stable phases that eventually form in this alloy. Understanding the critical connections in the structural hierarchy and the relative energetic and kinetic implications will lead to better ability to identify pathways for the realization of specific phases and structures that may not be accessible through conventional avenues.

ACKNOWLEDGMENTS

We would like to thank Jon Almer for his assistance with the HEXRD experiments. Work at Ames Laboratory was supported by the US Department of Energy, Basic Energy Sciences, Materials Science Division and Engineering, under Contract No. DE-AC02-07CH11358, including a grant of computer time at the National Energy Research Supercomputing Center (NERSC) in Berkeley, CA. The high-energy x-ray experiments were performed at the XOR beamline (sector 1) of the Advanced Photon Source, Argonne National Laboratory, under Grant No. DE-AC02-06CH11357. Y.S. acknowledges support from China Scholarship Council (File No. 201406340015). Z.J.D. acknowledges support from the National Natural Science Foundation of China (No. 11574289). K.M.H. acknowledges support from USTC Qian-Ren B (1000-Talents Program B) fund.

[1] A. Inoue and A. Takeuchi, Mater. Sci. Eng. A **375-377**, 16 (2004).
[2] U. Koster, J. Meinhardt, S. Roos, and A. Rudiger, Mater. Sci. Forum **225-227**, 311 (1996).
[3] C. Li, J. Saida, and A. Inoue, Mater. Trans., JIM **41**, 1521 (2000).
[4] S. Brauer, J. O. Ström-Olsen, M. Sutton, Y. S. Yang, A. Zaluska, G. B. Stephenson, and U. Köster, Phys. Rev. B **45**, 7704 (1992).
[5] S. H. Kilcoyne, P. Manuel, and C. Ritter, J. Phys. Condens. Matter **13**, 5241 (2001).
[6] M. Yan, J. Q. Wang, C. Kong, G. B. Schaffer, and M. Qian, J. Mater. Res. **27**, 2131 (2012).
[7] D. J. Sordelet, E. Rozhkova, M. F. Besser, and M. J. Kramer, Appl. Phys. Lett. **80**, 4735 (2002).
[8] D. Raabe, M. Herbig, S. Sandlöbes, Y. Li, D. Tytko, M. Kuzmina, D. Ponge, and P.-P. Choi, Curr. Opin. Solid State Mater. Sci. **18**, 253 (2014).
[9] O. Heinen, D. Holland-Moritz, D. M. Herlach, and K. F. Kelton, J. Cryst. Growth **286**, 146 (2006).
[10] F. Zhang, M. Ji, X. W. Fang, Y. Sun, C. Z. Wang, M. I. Mendelev, M. J. Kramer, R. E. Napolitano, and K. M. Ho, Acta Mater. **81**, 337 (2014).
[11] Y. Sun, F. Zhang, Z. Ye, Y. Zhang, X. Fang, Z. Ding, C.-Z. Wang, M. I. Mendelev, R. T. Ott, M. J. Kramer, and K.-M. Ho, Sci. Rep. **6**, 23734 (2016).
[12] M. Imafuku, S. Sato, H. Koshiba, E. Matsubara, and A. Inoue, Mater. Trans. JIM **41**, 1526 (2000).
[13] J. Saida, M. Sherif El-Eskandarany, and A. Inoue, Scr. Mater. **48**, 1397 (2003).
[14] L. Battezzati, M. Baricco, P. Schumacher, W. C. Shih, and A. L. Greer, Mater. Sci. Eng. **179**, 600 (1994).
[15] Y. E. Kalay, C. Yeager, L. S. Chumbley, M. J. Kramer, and I. E. Anderson, J. Non-Cryst. Solids **356**, 1416 (2010).
[16] P. Rizzi, M. Baricco, S. Borace, and L. Battezzati, Mater. Sci. Eng. A **304-306**, 574 (2001).
[17] A. Inoue, Prog. Mater. Sci. **43**, 365 (1998).
[18] G. Tan, F. Shi, S. Hao, L. Zhao, H. Chi, X. Zhang, C. Uher, C. Wolverton, V. P. Dravid, and M. G. Kanatzidis, Nat. Commun. **7**, 12167 (2016).
[19] A. K. Gangopadhyay and K. F. Kelton, Philos. Mag. A **80**, 1193 (2000).
[20] A. Inoue, K. Ohtera, Z. Tao, and T. Masumoto, Jpn. J. Appl. Phys. **27**, L1583 (1988).
[21] R. Bacewicz and J. Antonowicz, Scr. Mater. **54**, 1187 (2006).
[22] J. Q. Guo, K. Ohtera, K. Kita, J. Nagahora, and N. S. Kazama, Mater. Lett. **24**, 133 (1995).
[23] S. H. Zhou and R. E. Napolitano, Metall. Mater. Trans. A **39**, 502 (2008).
[24] Y. E. Kalay, L. S. Chumbley, M. J. Kramer, and I. E. Anderson, Intermetallics **18**, 1676 (2010).
[25] W. Kohn and L. J. Sham, Phys. Rev. **140**, A1133 (1965).
[26] G. Kresse and J. Furthmüller, Comput. Mater. Sci. **6**, 15 (1996).
[27] P. E. Blochl, Phys. Rev. B **50**, 17953 (1994).
[28] G. Kresse and D. Joubert, Phys. Rev. B **59**, 1758 (1999).
[29] J. P. Perdew, K. Burke, and M. Ernzerhof, Phys. Rev. Lett. **77**, 3865 (1996).
[30] See Supplemental Material at http://link.aps.org/supplemental/10.1103/PhysRevMaterials.1.055601 for Fig. S1, where diffraction peaks of the primitive cubic cell and body-centered cubic cell are shown.
[31] John H. Holland, *Adaptation in Natural and Artificial Systems: An Introductory Analysis with Applications to Biology, Control, and Artificial Intelligence* (University of Michigan Press, Ann Arbor, 1975).

[32] D. E. Goldberg, *Genetic Algorithms in Search, Optimization, and Machine Learning* (Addison-Wesley Professional, Boston, MA, 1989).
[33] F. Zhang, I. McBrearty, R. T. Ott, E. Park, M. I. Mendelev, M. J. Kramer, C. Z. Wang, and K. M. Ho, Scr. Mater. **81**, 32 (2014).
[34] Z. Ye, F. Zhang, Y. Sun, M. I. Mendelev, R. T. Ott, E. Park, M. F. Besser, M. J. Kramer, Z. Ding, C. Z. Wang, and K. M. Ho, Appl. Phys. Lett. **106**, 101903 (2015).
[35] M. Ji, C.-Z. Wang, and K.-M. Ho, Phys. Chem. Chem. Phys. **12**, 11617 (2010).
[36] A. R. Oganov and C. W. Glass, J. Chem. Phys. **124**, 244704 (2006).
[37] M. C. Nguyen, J.-H. Choi, X. Zhao, C.-Z. Wang, Z. Zhang, and K.-M. Ho, Phys. Rev. Lett. **111**, 165502 (2013).
[38] S. Plimpton, J. Comput. Phys. **117**, 1 (1995).
[39] M. W. Finnis and J. E. Sinclair, Philos. Mag. A **50**, 45 (1984).
[40] M. I. Mendelev, F. Zhang, Z. Ye, Y. Sun, M. C. Nguyen, S. R. Wilson, C. Z. Wang, and K. M. Ho, Model. Simul. Mater. Sci. Eng. **23**, 45013 (2015).
[41] H. M. Rietveld, J. Appl. Crystallogr. **2**, 65 (1969).
[42] R. A. Young, *The Rietveld Method* (Oxford University Press, New York, NY, 1993).
[43] B. H. Toby, J. Appl. Crystallogr. **34**, 210 (2001).
[44] C. Tang and P. Harrowell, Nat. Mater. **12**, 507 (2013).
[45] See Supplemental Material at http://link.aps.org/supplemental/10.1103/PhysRevMaterials.1.055601 for more details about the large-scale MD simulations.